Microstructure-based model of nonlinear ultrasonic response in materials with distributed defects

View Online   Export Citation   CrossMark

Yulan Li, [ID] Shenyang Hu,[a) [ID]] and Charles H. Henager, Jr. [ID]

AFFILIATIONS

Pacific Northwest National Laboratory, 902 Battelle Boulevard, Richland, Washington 99352, USA

[a)]**Author to whom correspondence should be addressed:** shenyang.hu@pnnl.gov

ABSTRACT

Nonlinear ultrasonic technique is one of several promising nondestructive evaluation methods for monitoring the evolution of nanosized defects such as radiation-induced defects in nuclear materials. In this work, a microstructure-based phase-field model of dynamic deformation in elastically nonlinear materials has been developed for investigating the dynamic interaction between distributed defects and a propagating longitudinal sound wave. With the model, the effect of second phase precipitates' size and properties on the nonlinearity parameter β that describes the magnitude of the 2nd harmonic wave was simulated. The results showed that (1) the nonlinearity parameter β increases as the elastic inhomogeneity increases regardless of whether the precipitates are softer or harder than the matrix; (2) β linearly increases with the increase of lattice mismatch strain; and (3) for a given volume fraction of second phase precipitates, β strongly depends on the precipitate size. The predicted precipitate size dependence of β agrees with the experimental data. These results demonstrate that the developed model enables one to predict the contributions of different nonlinear sources to β, to explain the signal physics behind the measured nonlinear ultrasonic response, and to guide the development of nonlinear ultrasound nondestructive detection of material defects in nuclear reactor materials.

I. INTRODUCTION

Ultrasonic inspection is a common nondestructive technique (NDT) used for locating cracks, corrosion layers, and other defects in structural components. Conventional linear ultrasonic techniques (UTs) rely on measuring parameters, such as sound velocity, attenuation, or transmission and reflection coefficients of the propagating signal, to determine the elastic properties of a material or to detect different scattering defects on the order of the wavelength of the ultrasonic wave. These UTs have been successfully applied to meet regulatory requirements for the inspection of primary loop components during commercial nuclear power reactor operation.[1] However, the conventional UT is primarily sensitive to gross material damage and cracks; there is limited evidence of their applicability in monitoring the accumulation of nanosized irradiation defects that are orders of magnitude smaller than the wavelength used in conventional UT.[2] A potential technique to overcome this limitation of the conventional ultrasonics is nonlinear ultrasonics (NLUS). Unlike the conventional UT, NLUS measurements are based on the fact that as a sinusoidal wave propagates through a nonlinear medium, a second harmonic wave is generated. The measured response is usually quantified in terms of the acoustic nonlinearity parameter, β,[3]

$$\beta = \frac{8A_2}{(A_1)^2 x k_L^2},\qquad(1)$$

where $k_L = \frac{2\pi}{\lambda_L}$ is the propagation vector or wave number with λ_L being the wavelength, x is the propagation distance, A_1 is the amplitude of the fundamental harmonic, and A_2 is the second harmonic amplitude.

In materials with radiation damage, the nonlinearity arises from lattice anharmonicity and microstructural features (composition and structure changes) such as dislocations, dislocation loops, precipitates, and voids as well as defect interactions such as the interactions between dislocations and precipitates. The use of NLUS as a diagnostic tool in materials science[4–14] and in materials monitoring activities[15–22] is an active and growing area of research.

Cantrell[9] discussed the use of β as a measure of fatigue damage in materials by computing the density effect of dislocation dipoles and fatigue cracks on β due to damage accumulation, and a model was developed that correlates β with the remaining fatigue life. Kim and Park[23] found an increase in β with the thermal aging of steel by correlating the increase in carbide densities and carbide structural changes. Very recently, Matlack et al.[22] demonstrated the sensitivity of NLUS to irradiation defects in a reactor pressure vessel (RPV) steel and suggested that material degradation can be characterized by $\beta(t)$. They further documented this by showing the dependence of β on neutron fluence, material composition, irradiation temperature, and annealing.[4] Thus, the use of NLUS as a real-time diagnostic tool to measure material degradation is warranted.

Parallel to NLUS experiments, some theoretical models have been developed to describe the effect of distributed defects on the β-parameter. Hikata et al.[24] developed a model to calculate the change of β due to distributed dislocations pinned by microstructural features such as grain boundaries, other dislocations, and/or point defects with internal stresses. Cantrell and Zhang[25] proposed a model to estimate the change of β due to dislocation networks pinned by coherent precipitates. Matlack et al.[4,22] used a "probability" concept to consider the effect of evolving microstructure (Cu precipitation under irradiation) on β. All the models are based on an average dislocation segment length, which depends on pinning defect density, and local stress, which causes dislocation bow-out. The developed theoretical models or/empirical formula could reasonably explain some microstructure dependence of β observed in experiments. However, in irradiated materials, the microstructure is complex. Different defects such as voids, second phase precipitates, dislocation loops, and mobile dislocations coexist, which causes an overlapping of internal stresses with spatial inhomogeneous distributions due to their interaction. The existing models fail to consistently explain $\beta(t)$ evolution in irradiated materials[4] because of the complex microstructures and coupling effects.

In spite of the research to date on NLUS, a noted *gap* is the ability to decode NLUS signals, to establish the correlation between defects and NLUS signals, and to generate damage maps for diagnostics and prognostics. The unique advantage of the microstructural-based phase-field approach of dislocation dynamics[26–30] is the ability to consider the interactions of evolving dislocations and distributed defects under applied stresses. Compared to the theoretical models mentioned above, the phase-field model allows for relaxation of the assumption of uniform microstructures and uniform internal stresses and also conveniently allows for the study of individual defect and multiple defects on β. In this work, we developed a phase-field model of dynamic deformation in nonlinear materials with distributed defects for investigating the dynamic interaction between propagating ultrasonic waves and defects and for exploring the relationship between distributed defects and β.

II. EQUATIONS OF DYNAMIC DEFORMATION IN MATERIALS WITH NONLINEARITY AND DEFECTS

We consider an elastically heterogeneous nonlinear solid containing defects such as precipitates, interstitial loops, vacancy loops, and dislocations, as shown in Fig. 1. These are common defects observed in irradiated materials in nuclear reactors. For example,
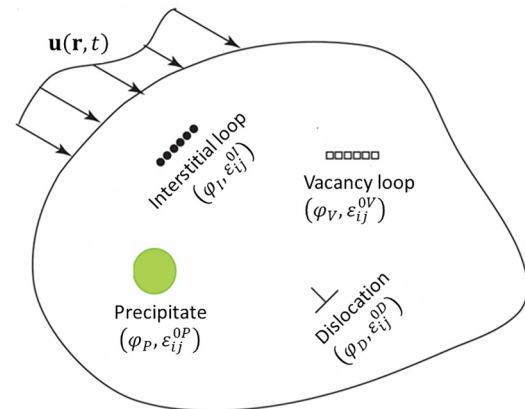

FIG. 1. A schematic illustration of a nonlinear elastic solid containing various defects that are described by phase-field order parameters $\varphi_m(\mathbf{r})$ and mismatch strains ε_{ij}^{0m}.

in irradiated Fe-Cu alloys, typical defects include vacancies, interstitials and their clusters, interstitial loops, vacancy loops, Cu precipitates, and voids. To describe the inhomogeneous thermal-mechanical properties such as elastic constants and mass in different phases and the lattice mismatch between matrix and defects, a set of order parameters $\varphi_m(\mathbf{r})$ ($m = P$, I, V, and D) are used to describe the spatial distribution of defects where $\mathbf{r} = (x_1, x_2, x_3)$ is the spatial coordinate. $\varphi_m(\mathbf{r})$ is equal to 1 inside the defects of type m, and 0 outside of the defects of type m, while it varies smoothly from 1 to 0 across the interfaces of the defects. The order parameter $\varphi_m(\mathbf{r})$ can be read directly from the images of microstructures or generated by phase-field simulations.[31] The spatial dependent stress-free strains associated with the lattice mismatches between the distributed defects and matrix as shown in Fig. 1 can be described by $\varepsilon_{ij}^0(\mathbf{r}) = \sum_{m=P,I,V,D} \varepsilon_{ij}^{0m} \varphi_m(\mathbf{r})$, where ε_{ij}^{0m} are the stress-free strains associated with the defects of type m. Other material properties such as mass and elastic constants can be described in a similar way.

To investigate how these defects affect the NLUS responses, we need to solve dynamic deformation equations in a nonlinear elastic solid with defects. The elastic nonlinearity discussed here is assumed to be from physics, not from a large nonlinear deformation. Therefore, the elastic potential can be described as[32,33]

$$W = \frac{1}{2}\lambda\left(\sum_{m=1}^{3}\varepsilon_{mm}\right)^2 + \mu\sum_{k=1}^{3}\sum_{i=1}^{3}(\varepsilon_{ik}\varepsilon_{ki})$$
$$+ \frac{1}{3}A\sum_{m=1}^{3}\sum_{i=1}^{3}\sum_{k=1}^{3}(\varepsilon_{ik}\varepsilon_{km}\varepsilon_{mi}) + B\left[\sum_{k=1}^{3}\sum_{i=1}^{3}(\varepsilon_{ik}\varepsilon_{ki})\right]\sum_{m=1}^{3}\varepsilon_{mm}$$
$$+ \frac{1}{3}C\left(\sum_{m=1}^{3}\varepsilon_{mm}\right)^3, \tag{2}$$

where ε_{ik} is the elastic strain, λ and μ are the elastic Lame parameters, and A, B, and C are the nonlinear elastic constants. $A = B = C = 0$

corresponds to the linear case. All the elastic constants are spatially dependent and associated with the elastic constants of different phases and their spatial distribution. The stress σ_{ik} ($i, k = 1, 2, 3$) can be obtained by

$$\sigma_{ik} = \frac{\partial W}{\partial \varepsilon_{ik}}, \tag{3}$$

which results in

$$\sigma_{ij} = \lambda \delta_{ij} \sum_{k=1}^{3} \varepsilon_{kk} + 2\mu \varepsilon_{ij} + \sigma_{ij}^{nl}, \tag{4}$$

where

$$\sigma_{ij}^{nl} = A \sum_{k=1}^{3} \varepsilon_{ik}\varepsilon_{kj} + B \left(\delta_{ij} \sum_{k=1}^{3} \sum_{l=1}^{3} \varepsilon_{kl}^2 + 2\varepsilon_{ij} \sum_{k=1}^{3} \varepsilon_{kk} \right) + C\delta_{ij} \left(\sum_{k=1}^{3} \varepsilon_{kk} \right)^2. \tag{5}$$

The equations of dynamic deformation (balance equations of impulse) are formulated by

$$\rho \frac{\partial^2 u_i}{\partial t^2} = \sum_{j=1}^{3} \frac{\partial \sigma_{ij}}{\partial x_j} + f_i \ (i = 1, 2, 3), \tag{6}$$

where ρ is the spatial dependent mass density, and f_i ($i = 1, 2, 3$) are the external body force components. We assumed $f_i = 0$ in this work. u_i ($i = 1, 2, 3$) are the displacement components. They are related to the elastic strains ε_{ik}($i, k = 1, 2, 3$) as

$$\varepsilon_{ik} = \frac{1}{2}(u_{i,k} + u_{k,i}) - \varepsilon_{ik}^0 \ (i, k = 1, 2, 3), \tag{7}$$

where ε_{ik}^0 are the spatial dependent eigenstrain stress-free strain tensor and are associated with the lattice mismatch between defects and the matrix.[34]

We use a bcc-Fe matrix with distributed Cu precipitates as a model system to illustrate the inhomogeneous quantities associated with the nonlinear dynamic model described above. Experiments show that when Cu precipitates are less than 5 nm in diameter, the Cu precipitates have the same bcc crystal structure as that of the matrix.[35] The stress-free strain tensor of Cu precipitates can be described as $\varepsilon_{ij}^{0P} = ((a_0^{Fe} - a_0^{Cu})/a_0^{Cu})\delta_{ij}$, where δ_{ij} is the Kronecker-Delta function and a_0^{Cu} and a_0^{Fe} are the lattice constants of bcc-Cu and bcc-Fe, respectively. Then, the eigenstrain associated with precipitate distribution can be written as

$$\varepsilon_{ij}^0(\mathbf{r}) = \varepsilon_{ij}^{0P}\varphi_P(\mathbf{r}) = \frac{a_0^{Fe} - a_0^{Cu}}{a_0^{Cu}}\delta_{ij}\varphi_P(\mathbf{r}), \tag{8}$$

where the function $\varphi_P(\mathbf{r})$ describes the spatial distribution of the precipitates with $\varphi_P(\mathbf{r}) = 1$ inside the precipitates, while $\varphi_P(\mathbf{r}) = 0$ outside the precipitates. In a similar way, the lattice mismatch of dislocations and dislocation loops can also be described by an eigenstrain tensor.[36,37]

The material constants can be decomposed as

$$\rho(\mathbf{r}) = \rho_0 + \rho_1\varphi_P(\mathbf{r}), \tag{9}$$

$$\lambda(\mathbf{r}) = \lambda_0 + \lambda_1\varphi_P(\mathbf{r}), \quad \mu(\mathbf{r}) = \mu_0 + \mu_1\varphi_P(\mathbf{r}), \tag{10}$$

where ρ_0, λ_0, and μ_0 are the elastic constants of the matrix Fe and ρ_1, λ_1, and μ_1 are the increments of elastic constants of bcc-Cu precipitates compared to the matrix Fe. Therefore, the equations of dynamic deformation can be written as

$$\rho \frac{\partial^2 u_i}{\partial t^2} - \mu_0 \sum_{k=1}^{3} \frac{\partial^2 u_i}{\partial x_k^2} - (\lambda_0 + \mu_0) \sum_{k=1}^{3} \frac{\partial^2 u_k}{\partial x_i \partial x_k} = F_i, \tag{11}$$

where $F_i = F_i(\lambda, \mu, u_{k,l}, \varepsilon_{kl}^0)$ ($i = 1, 2, 3$) are composed of the nonlinear and heterogeneous materials and eigenstrains. In detail,

$$F_i = \sum_{k=1}^{3} \frac{\partial}{\partial x_k}[-\sigma_{ik}^0 + \sigma_{ik}^{inh} + \sigma_{ik}^{nl}], \quad i = 1, 2, 3 \tag{12}$$

and

$$\sigma_{ij}^{inh} = \lambda_1\delta_{ij} \sum_{k=1}^{3} \varepsilon_{kk} + 2\mu_1\varepsilon_{ij}, \tag{13}$$

$$\sigma_{ij}^0 = \lambda_0\delta_{ij} \sum_{k=1}^{3} \varepsilon_{kk}^0 + 2\mu_0\varepsilon_{ij}^0. \tag{14}$$

Equation (12) clearly shows that material heterogeneity and eigenstrains or eigenstresses have similar contributions as the material nonlinearity in Eq. (11). This implies that material heterogeneity and eigenstrains can cause higher-order harmonic generation in the same manner as the material nonlinearity. Therefore, any material heterogeneity and lattice mismatch associated with irradiation defects will affect β.

In a simplified one-dimensional (1D) case where $\sigma_{ij}^0 = 0$, $u_2 = 0$, $u_3 = 0$, $\lambda_1 = 0$ and $\mu_1 = 0$ so $\sigma_{ij}^{inh} = 0$, only $u_1 = u_1(x_1, t)$ is not zero, and Eq. (11) becomes

$$\rho_0 u_{1,tt} - (\lambda_0 + 2\mu_0)u_{1,11} = -N_1 u_{1,1}u_{1,11}, \tag{15}$$

with

$$N_1 = -2(A + 3B + C). \tag{16}$$

We rewrite Eq. (15) as

$$u_{1,tt} - (v_L)^2 u_{1,11} = -\beta(v_L)^2 u_{1,11}u_{1,1}, \tag{17}$$

where v_L is the longitudinal wave velocity in the material

$$v_L = \sqrt{\frac{\lambda_0 + 2\mu_0}{\rho_0}}, \tag{18}$$

and β is termed the nonlinearity parameter and is defined as

$$\beta = \frac{\left(\frac{N_1}{\rho_0}\right)}{(v_L)^2} = \frac{N_1}{(\lambda_0 + 2\mu_0)}. \tag{19}$$

The solution of Eq. (17) can be obtained by the perturbation method or by the method of successive approximations.[32] The solution in the forms of the first two approximations is as follows:

$$u_1 = A_1 \cos(k_L x_1 - \omega t) - A_2 \cos 2(k_L x_1 - \omega t) + \cdots, \qquad (20)$$

with

$$A_2 = \frac{1}{8}\beta(A_1)^2 x_1 k_L^2 \qquad (21)$$

and

$$k_L = \frac{\omega}{v_L}. \qquad (22)$$

The solution in Eq. (20) shows that an initial wave with frequency ω propagates without a change in linear materials ($A = B = C = 0$). Due to the material nonlinearity when the material constants A, B, and C are nonzero, however, a second harmonic wave is generated. With increasing wave propagation distance, the effect of the second harmonic increases and dominates. The solution of Eq. (17) also validates theoretically that the second harmonic generation is due to the nonlinear elastic properties related to intrinsic elastic nonlinearity and defects (elastic inhomogeneity and lattice mismatch). In turn, it can be used to detect defects through measuring β. Therefore, if the material property, N_1, is known, β can be calculated from Eq. (19). On the other hand, if N_1 is unknown, β can be obtained through $\beta = 8A_2/(A_1)^2 x_1 k_L^2$ by measuring A_1 and A_2, the amplitudes of the first and second harmonic waves, respectively.

III. NUMERICAL SOLUTION AND MODEL PARAMETER VALIDATION

By solving Eq. (11) under given boundary and initial conditions, we can obtain the displacement vector $\mathbf{u} = (u_1, u_2, u_3)$ varying with time. To numerically solve Eq. (11), a forward Euler scheme and a central difference method were used for calculating the first- and second-order derivatives with respect to time, respectively, i.e.,

$$\mathbf{v} = \frac{d\mathbf{u}}{dt} = \frac{\mathbf{u}^{t+\Delta t} - \mathbf{u}^t}{\Delta t}, \frac{d^2\mathbf{u}}{dt^2} = \frac{d\mathbf{v}}{dt} = \frac{\mathbf{u}^{t+\Delta t} - 2\mathbf{u}^t + \mathbf{u}^{t-\Delta t}}{(\Delta t)^2}, \quad (23)$$

where $\mathbf{v}$ is the speed vector and Δt is the time step. The superscripts $t+\Delta t$, t, and $t - \Delta t$ refer to the corresponding time moments, respectively. The semi-implicit Fourier spectral method is employed for spatial discretization.[38] Iteration[39] was used to deal with the nonlinearity and heterogeneity, i.e., the right hand side of Eq. (11). Once the solutions at t and $t - \Delta t$, i.e., $\mathbf{u}^t$ and $\mathbf{u}^{t-\Delta t}$ are obtained,

the solution $\mathbf{u}^{t+\Delta t}$ at $t + \Delta t$ is solved as

$$\rho_0 \frac{u_i^{t+\Delta t}}{(\Delta t)^2} - \mu_0 \sum_{k=1}^{3}\frac{\partial^2 u_i^{t+\Delta t}}{\partial x_k^2} - (\lambda_0 + \mu_0)\sum_{k=1}^{3}\frac{\partial^2 u_k^{t+\Delta t}}{\partial x_i \partial x_k}$$
$$= -\rho_1 \frac{u_i^{t+\Delta t}}{(\Delta t)^2} - \rho\frac{-2u_i^t + u_i^{t-\Delta t}}{(\Delta t)^2} + F_i^{t+\Delta t}. \qquad (24)$$

We used an iteration process to numerically solve Eq. (24) at time step $t + \Delta t$ as

$$\rho_0 \frac{u_{i,m}^{t+\Delta t}}{(\Delta t)^2} - \mu_0 \sum_{k=1}^{3}\frac{\partial^2 u_{i,m}^{t+\Delta t}}{\partial x_k^2} - (\lambda_0 + \mu_0)\sum_{k=1}^{3}\frac{\partial^2 u_{k,m}^{t+\Delta t}}{\partial x_i \partial x_k}$$
$$= -\rho_1 \frac{u_{i,m-1}^{t+\Delta t}}{(\Delta t)^2} + F_{i,m-1}^{t+\Delta t} - \rho\frac{-2u_i^t + u_i^{t-\Delta t}}{(\Delta t)^2}, \qquad (25)$$

where the subscript, m, represents the iteration step, and $m = 1, \ldots, M$. When $m = 1$, $\mathbf{u}_{m-1}^{t+\Delta t} = \mathbf{u}_0^{t+\Delta t} = \mathbf{u}^t$. When $|\mathbf{u}_M^{t+\Delta t} - \mathbf{u}_{M-1}^{t+\Delta t}| \leq criterion$, $\mathbf{u}^{t+\Delta t} = \mathbf{u}_M^{t+\Delta t}$ is the solution at $t + \Delta t$.

In this work, we studied the nonlinear response from different sources including the material nonlinearity described by constants A, B, and C in Eq. (2), heterogeneity due to $\rho_1(\mathbf{r})$, $\lambda_1(\mathbf{r})$, and $\mu_1(\mathbf{r})$ in Eqs. (9) and (10), and eigenstrains $\varepsilon_{ik}^0(\mathbf{r})$ in Eq. (7). The heterogeneity or eigenstrains are associated with distributed precipitates/particles. The simulations were conducted in a physical domain (or a simulation cell) of $8192l_0 \times 16l_0 \times 16l_0$ illustrated in Fig. 2, where l_0 is the characteristic length and taken to be 1 nm for the following simulations. A periodic boundary condition is applied to both x_2 and x_3 directions.

IV. MODEL PARAMETER VALIDATION

To validate the model and numerical methods, we first simulated the effect of the wave amplitude, wavelength, and material nonlinearity on β and analyzed the numerical accuracy by comparing with the analytical solution. A composite with copper particles and a molybdenum matrix[40] was taken as a model material, where the material nonlinearity is described by nonlinear elastic constants A, B, and C. Table I lists the used material constants and model parameters. In the simulation, an initial wave of $u_1(x_1, x_2, x_3; t = 0) = u_0 \cos[k_L(x_1 + n_L/2 - x_0)]$ in the source region $x_0 - 2n_L \leq x_1 \leq x_0 + 2n_L$ was introduced by displacing the material along x_1 sinusoidally. The initial wave has two wavelengths with the wave number $k_L = \frac{2\pi}{2n_L}$ and propagates along the x_1 direction from point P_1. A detector is set at point P_2 to record the average displacement of the plane ($x_2 x_3$) at P_2. The distance
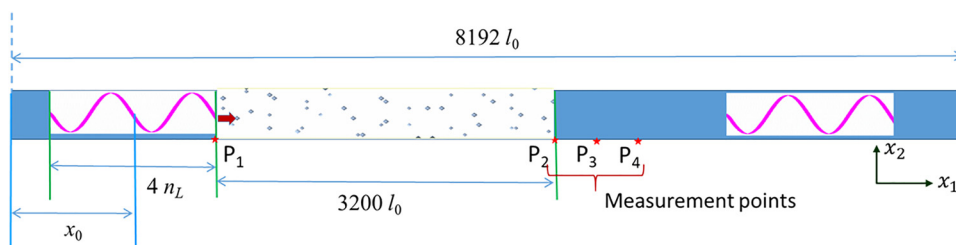

FIG. 2. Schematic illustration of the simulation cell on the $x_1 x_2$ plane. The 3D simulation cell has dimensions $8192l_0 \times 16l_0 \times 16l_0$, where l_0 is the characteristic length. The distributed particles denote precipitates or voids. The red star points denote the planes where the displacements are recorded for analyzing wave propagation.

TABLE I. Material constants[32] and model parameters used in the simulations.

Properties	Parameters	Values
Shear modulus	μ_0	94.1 GPa
Density	ρ_0	9950 kg/m^3
Lame parameter	λ_0	145 GPa
Nonlinear modulus	A_0	-124 GPa
Nonlinear modulus	B_0	-252 GPa
Nonlinear modulus	C_0	-350 GPa
$-2(A_0 + 3B_0 + C_0)$	N_1	2460 GPa
$\frac{N_1}{(\lambda_0 + 2\mu_0)}$	β	7.383
Wavespeed $\sqrt{\frac{\lambda_0 + 2\mu_0}{\rho_0}}$	v_L	5687.83 m/s
Characteristic length	l_0	10^{-9} m
Half wavelength	n_L	$400 l_0 = 4 \times 10^{-7}$ m
Wavelength $2n_L$	λ_L	8.0×10^{-7} m
Angular frequency $\frac{2\pi v_L}{\lambda_L}$	ω	45.45 GHz
Frequency $\frac{\omega}{2\pi}$	f	7.234 GHz
Wave number $\frac{\omega}{v_L} = \frac{2\pi}{\lambda_L}$	k_L	7.854×10^6/m
Characteristic time $\sqrt{\frac{\rho_0 l_0^2}{\mu_0}}$	t_0	3.252×10^{-13} s
	$1/t_0$	3.075×10^{12}/s
Normalized frequency $f t_0$	$f^\star$	0.00235
Numerical error	$Criterion$	1×10^{-5}

between P_1 and P_2 is $3200 l_0$. The acquired displacement was used for the fast Fourier transform (FFT) analysis to obtain the amplitudes of the fundamental wave and the second harmonic wave at the plane.

The recorded displacement at P_2 for the initial wave with $n_L = 400 l_0$ and $u_0 = 0.05 l_0$ is depicted in Fig. 3(a). The time step $\Delta t = 0.005 t_0$ and iteration $M = 1$ were used in the simulations. The displacement within one period, shown in red in Fig. 3(a), was used to do nonlinearity analysis through FFT. The obtained A_1 and A_2, i.e., the amplitudes of the first and second harmonic waves, are plotted in Fig. 3(b). With the initial wave and simulation cell setup, and the described FFT analysis approach, in the following we validate our model and numerical accuracy by examining the effect of the initial wave amplitude u_0, wavelength $\lambda_L = 2n_L$, and the material constant N_1 on β.

A. Effect of amplitude u_0

Different amplitudes u_0 were used to examine its effect on β, which is calculated by $\beta = \frac{8A_2}{(A_1)^2 x_1(P_2) k_L^2}$, where $x_1(P_2) = 3200 l_0 + \lambda_L$. The obtained results are displayed in Fig. 4 and Table II. Figure 4 shows the plot of $(A_1)^2$ vs A_2 with varying u_0. It is seen that $(A_1)^2$ is linear to A_2 when the ampliyude u_0 varies monotonously. The analytical solution (19) is $\beta_0 = \frac{N_1}{(\lambda_0 + 2\mu_0)} = 7.383$ for the given material properties, which is independent of the amplitude u_0. The difference $\left| \frac{\beta - \beta_0}{\beta_0} \right|$ between the calculated and analytical solutions is also listed in Table II. It can be seen that β slightly decreases as the amplitude u_0 increases. However, when $0.01 \leq u_0/l_0 \leq 0.5$, the numerical error is less than 2%. The numerical error could be reduced by reducing the characteristic length l_0 (or increasing the simulation cell size) and/or
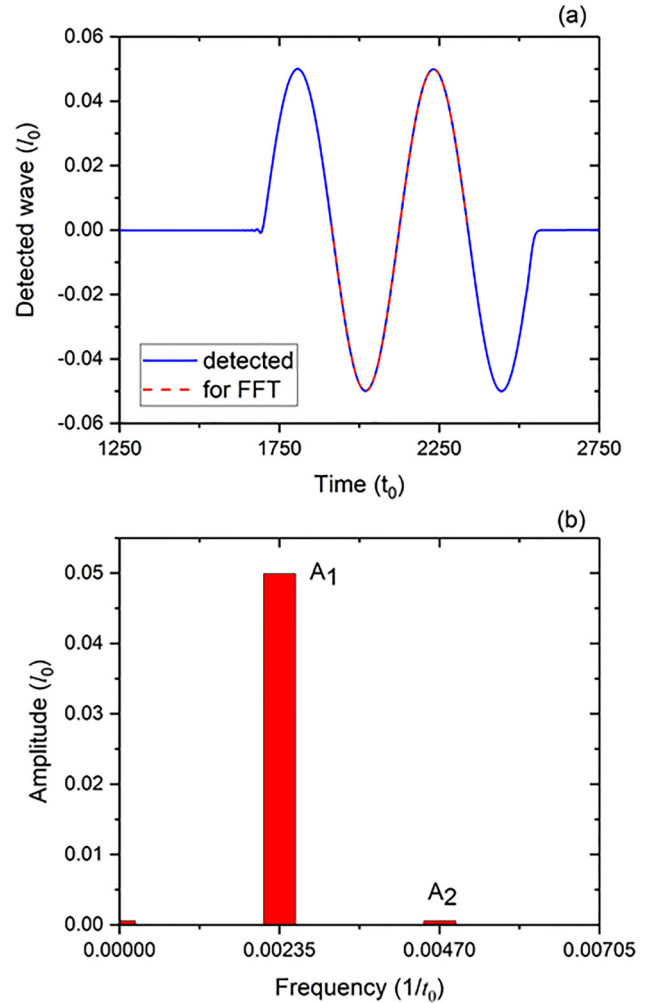
FIG. 3. (a) Recorded displacement at P_2 for the initial wave with $\lambda_L = 800 l_0$ and $u_0 = 0.05 l_0$ and (b) amplitude spectrum from FFT analysis.

reducing the time step Δt. In the following simulations, $\frac{u_0}{l_0} = 0.05$ is taken.

B. Effect of wavelength λ_L

The effect of wavelength $\lambda_L = 2n_L$ on β is listed in Table III. We can see that the calculated β approaches the analytical solution β_0 with increasing wavelength λ_L. For wavelength $n_L/l_0 = 150 \sim 400$, the numerical error is less than 2%. It should be pointed out that for a given l_0, increasing the wavelength increases the size of simulation cell in the x_1 direction.

C. Effect of constant N_1

It is known from Eq. (19) that β is proportional to the material constant N_1 such that a larger N_1 increases β. Table IV gives
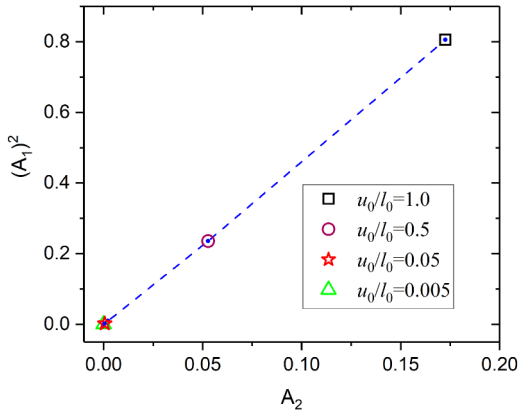
FIG. 4. $(A_1)^2$ vs A_2 when u_0 varying from $0.005l_0$ to $1.0l_0$ as listed in Table II.

the comparison between the calculated β and the analytical $\beta_m = N_1/(\lambda_0 + 2\mu_0)$ for different material constant N_1. The results show that the numerical error decreases with increasing N_1, i.e., nonlinearity. The numerical error is less than 2% when β is larger than 0.738. A comparison between the analytical β_m and the calculated β with the developed method is plotted in Fig. 5.

The above validation demonstrates that model parameters and material properties do affect the accuracy of the numerical solution. However, a numerical solution that is less than 2% numerical error can be obtained with our model parameters and the developed model can predict the nonlinearity parameter β for the used model parameters: $0.01 \leq u_0/l_0 \leq 0.5$, wavelength $n_L/l_0 = 150 \sim 400$, $\Delta t/t_0 = 0.005$.

V. EFFECT OF DISTRIBUTED PARTICLES ON NONLINEARITY PARAMETERS

Radiation-induced precipitate hardening is an important material property degradation mechanism in Fe-Cu alloys. High-resolution electron microscopy experiments have revealed that a Cu precipitate in bcc-Fe undergoes bcc $\rightarrow$ 9R transformation when the diameter of the precipitate is larger than the critical size.[41,42] The Cu precipitates have different material properties from the Fe matrix, and eigenstrains associated with the lattice mismatch between bcc-Cu and bcc-Fe lattices and/or structure change

from bcc to 9R. In addition, the size of Cu precipitates increases with increasing aging and/or radiation time, while the volume fraction remains the same. In this section, we study the effect of particle size, eigenstrains ε_{ij}^0, and material properties such as mass m_1 and elastic constants μ_1 and λ_1 on β. For the sake of simplicity, it is assumed that (1) the particles are randomly distributed in a range with a width of $3200l_0$ as shown in Fig. 2; (2) they are spherical and have the same radius; and (3) the overall volume fraction of particles is a constant at 1%. A field variable $\varphi_P(\mathbf{r})$ is used to describe the particle distribution as well as the heterogeneous material properties as mentioned in Sec. II. $\varphi_P(\mathbf{r}) = 1$ represents particles, and $\varphi_P(\mathbf{r}) = 0$ represents the matrix. $\varphi_P(\mathbf{r})$ varies smoothly from 1 to 0 across the interfaces between particles and the matrix. Thus, the material properties and eigenstrains are continuous across the interfaces, which can improve the numerical accuracy and efficiency. The field variable $\varphi_P(\mathbf{r})$ is obtained by a phase-field model of precipitation.[43] For a given particle radii with a constant volume fraction of 1%, the number of particles within the simulation zone of $3200l_0$ is listed in Table V.

Considering the facts that (1) different spatial distributions of particles might affect the displacement on the plane at P_2, especially if the simulation cell is not large enough, and (2) the nonlinearity and inhomogeneity might generate higher-order harmonic waves, while Eq. (1) is applicable only if the higher-order harmonic term is negligible compared to the second harmonic term, we recorded the displacements of three different planes at P_2, P_3, and P_4 shown in Fig. 2. The distance between any neighboring points is $100l_0$. In the calculation of nonlinearity, we used only those displacements where the amplitude of any harmonic waves higher than the 2nd harmonic wave is negligible compared to that of the 2nd harmonic wave.

TABLE II. Calculated $\beta = \frac{8A_2}{(A_1)^2 x_1(P_2)k_L^2}$ vs u_0.

u_0/l_0	β	$\left\|\frac{\beta - \beta_0}{\beta_0}\right\|$
0.005	7.5747	0.0260
0.01	7.4687	0.0116
0.02	7.4223	0.0053
0.05	7.3956	0.0017
0.1	7.3827	0.00004
0.5	7.2562	0.0172
1.0	6.9450	0.0593

TABLE III. Calculated $\beta = \frac{8A_2}{(A_1)^2 x_1(P_2)k_L^2}$ vs wavelength $\lambda_L = 2n_L$ with $\frac{u_0}{l_0} = 0.05$.

n_L/l_0	β	$\left\|\frac{\beta - \beta_0}{\beta_0}\right\|$
100	7.0454	0.0457
150	7.2756	0.0145
200	7.3625	0.00278
250	7.3794	0.0031
300	7.3752	0.00106
350	7.3749	0.0011
400	7.3809	0.000284

TABLE IV. Nonlinearity parameter β vs the material constant N_1 with $\frac{u_0}{l_0} = 0.05$ and $\frac{n_L}{l_0} = 400$.

N_1 (GPa)	$\beta_m = \frac{N_1}{(\lambda_0 + 2\mu_0)}$	$\beta_{cal} = \frac{8A_2}{(A_1)^2 x_1(P_2)k_L^2}$	Error: $\frac{\beta_{cal} - \beta_m}{\beta_m}$
2460	7.383	7.3809	0.00028
1968	5.9064	5.9208	0.00244
1476	4.4298	4.4436	0.00312
984	2.9532	2.9624	0.00312
246	0.7383	0.7523	0.0189
36.9	0.1107	0.1282	0.1581
0.0	0.0	0.0304	
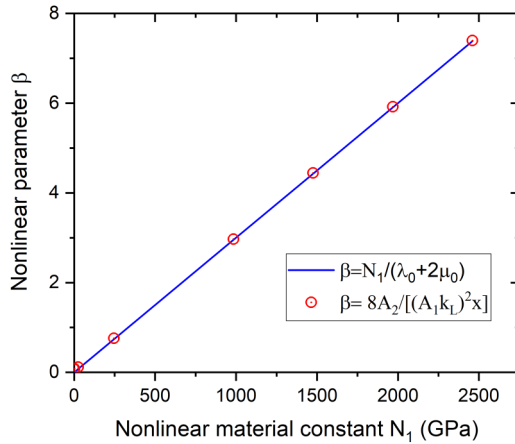
FIG. 5. β vs material's nonlinearity constant $N_1 = -2(A + 3B + C)$.

FIG. 6. β vs particle sizes and eigenstrains.

A. Effect of particle radius and eigenstrain on the NLUS response

Coherent particles such as bcc-Cu precipitates in bcc-Fe and crystal defects such as vacancies, interstitials, interstitial loop, vacancy loops, and dislocations cause lattice mismatch with the matrix and give rise to internal stress fields. These lattice mismatches can be described by an eigenstrain tensor or stress-free strain tensor.[34] The interaction between propagating ultrasonic wave and defect stress fields generates higher-order harmonic waves. In the simulation, we assumed that (1) the particles have eigenstrains of $\varepsilon_{11}^0 = \varepsilon_{22}^0 = \varepsilon_{33}^0 = \varepsilon_0$ and $\varepsilon_{12}^0 = \varepsilon_{23}^0 = \varepsilon_{13}^0 = 0.0$, which describes an isotropic lattice mismatch like bcc-Cu precipitates in a bcc-Fe matrix; and (2) matrix has a linear elasticity, i.e., $A = B = C = 0$. The initial waves with $n_L = 400l_0$ and $u_0 = 0.05l_0$ were used. The effects of eigenstrain ε_0 and particle sizes on ultrasonic wave propagation were simulated, respectively. Through analyzing the recorded displacement as described in Sec. III, we can obtain parameter β. Figure 6 shows β vs particle radius for given eigenstrains 0.01 and 0.005, respectively. The dashed blue line shows the intrinsic parameter β for the nonlinear materials with $N_1 = 2460$ GPa. We can see that eigenstrain-induced nonlinearity parameter has the same order as the intrinsic nonlinearity parameter.

TABLE V. Radii and numbers for considered particles.

Radius (nm)	Number of particles
0.9982	1970
1.5243	561
1.7825	357
2.0221	235
2.2540	170
2.5489	124
2.7729	92
2.9876	74

Note that the overall particle volume fraction is 1% for different particle sizes. Therefore, with increasing particle size, the particle density decreases as shown in Table V. The results show that when the particle size is less than about 2.5 nm in diameter, the nonlinearity parameter β increases with decreasing particle size and increasing particle density. When the particle size is larger than about 5.0 nm in diameter, the nonlinearity parameter β decreases with increasing particle size and decreasing particle density. When the particle size is between 2.5 nm and 5 nm, β increases with increasing particle size and decreasing particle density. MD simulations[44] investigated the effect of solute Cu and small Cu clusters on the nonlinearity parameter β in Fe-Cu alloys and showed that β decreases during Cu precipitation. It is consistent with the results shown in Fig. 6 when the particle size is less than about 2.5 nm in diameter. Nonlinear ultrasonic experiments also show similar results for larger Cu precipitates in Fe and β increases, then decreases with the increasing Cu particle sizes in annealed samples of Cu-Fe alloys.[45] Since the nonlinearity parameters calculated by atomistic simulations and measured in experiments include the multiple contribution such as intrinsic nonlinearity, phase transition of large Cu precipitates, and interactions between dislocations and Cu precipitates, we could not compare the absolute value of nonlinearity parameters from atomistic simulation, current model, and experiments. But the changes of β vs particle sizes from three different methods are in a reasonable agreement.

Figure 7 shows that β is a function of eigenstrain. It is interesting to find that β is proportional to the value of eigenstrain for the given particle size. The eigenstrains of bcc-Cu precipitates in bcc-Fe matrix are reported by the embedded atom method (EAM) and *ab initio* calculations.[46,47] Including experimental values,[48,49] the eigenstrain ranges from 0.01 to 0.03. For perfect bcc-Fe, MD simulations[44] showed that the intrinsic nonlinearity parameter for a longitudinal sound wave propagating along the [100] crystal direction was $\beta_0 = 2.73$. It is seen that the precipitates with eigenstrain of 0.01 resulted in a nonlinearity parameter of about 5.0. Furthermore, as we know, bcc-Cu precipitates transform to fcc as the particle size increases. As a result, eigenstrains vanish and the
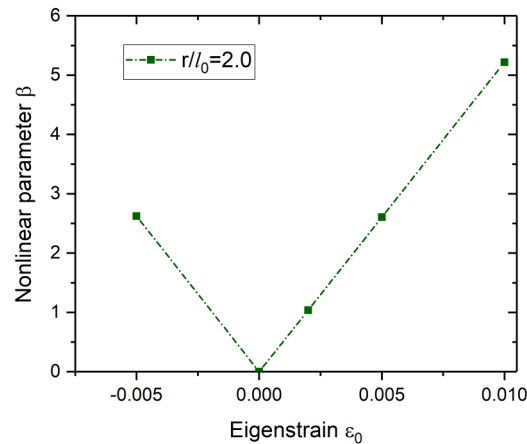
FIG. 7. β vs eigenstrain ε_0 for the case where the particles have a radius of $2.0l_0$.

coherent interface becomes semicoherent or incoherent.[35,42] It is expected that such a structure change would cause a large decrease in β. The simulations indicate that the formation of bcc-Cu precipitates in bcc-Fe may cause a large increase of nonlinearity, while the structure transition from bcc to 9R then to fcc Cu precipitates may reduce the nonlinearity. This information can be used to correlate ultrasonic signals with Cu precipitate sizes and structure change.

B. Effect of particle property on the NLUS response

Second phase particles usually have different densities and elastic constants compared to the matrix. Equations (9)–(11) show that the inhomogeneity of density and elastic constants affect wave propagation, hence, β. In this section, we considered the effect of density ρ_1 and elastic constants (μ_1, λ_1) on the NLUS response. The initial wave has a wavelength of $n_L = 400l_0$ and a magnitude
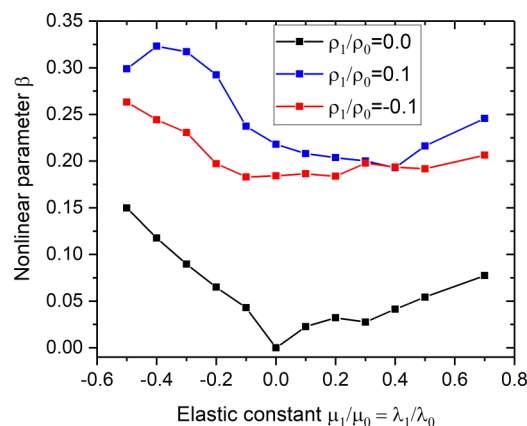

FIG. 8. Effect of density and elastic constants of precipitates on β.

of $u_0 = 0.05l_0$. The radii of the considered particles are about $2.0l_0$. The simulation results are plotted in Fig. 8 and show that the nonlinearity parameter β increases as the precipitates become harder $(\mu_1 > 0)$ or softer $(\mu_1 < 0)$ when the material density is constant. Softer precipitates have a greater impact on β than harder precipitates. Atomic simulations[46,47] showed that elastic shear modulus of bcc-Cu and bcc-Fe are about 145 GPa and 112 GPa, respectively. For bcc-Cu precipitates, μ_1/μ_0 is about 0.19, and the inhomogeneous elasticity causes about an increase of the nonlinearity parameter of 0.05 from Fig. 8. Compared with the effect of lattice mismatch on the nonlinearity parameter, the inhomogeneous elasticity has a weak impact. The inhomogeneous density also affects β that increases regardless of the sign of the density change. The value of ρ_1/ρ_0 for bcc-Cu precipitates in the bcc-Fe matrix is about 0.14. The results in Fig. 8 showed that both inhomogeneous density and elastic constants of the precipitates impact β. However, the impacts are much smaller than that caused by the lattice mismatch. The result is in agreement with the estimation in a review article.[2]

VI. CONCLUSIONS

A microstructure dependent model of dynamic deformation has been developed to study the effect of distributed defects on the 2nd order harmonic generation and the nonlinearity parameter β. The dynamic deformation equations indicate that the particle eigenstrains and inhomogeneous material properties have a function similar to that of nonlinear elasticity so the generation of higher-order harmonic waves is suggested. Simulations showed that (1) β linearly increases with increasing lattice mismatch; (2) β increases with an increase of elastic inhomogeneity regardless of whether the precipitates are softer or harder than the matrix; and (3) for the given volume fraction of second phase precipitates, β strongly depends on the precipitate size. The results imply that the large lattice mismatch associated with the formation of bcc-Cu precipitates in the bcc-Fe matrix should cause a large increase of β, while the reduction of the eigenstrain due to the structure transition from bcc to 9R to fcc Cu precipitates should cause a large decrease in β. Therefore, the simulation results could be used to correlate ultrasonic signals with the evolution of precipitate sizes and structure change.

In this work, we only considered the effect of inhomogeneous properties associated with defects on β; however, several other factors may contribute to β in real materials. For instance, grain boundaries, phase transitions, plastic deformation, and interactions among dislocations and defects can all cause the generation of 2nd order harmonic waves, hence, affect β. We also showed that phase-field methods have an advantage in coupling the elastic wave equations with microstructure evolution. Phase-field models of dislocation dynamics can quantitatively describe dislocation glide, dislocation reactions, and defect pinning.[26–30] With this capability, the developed model can be extended to consider dislocation dynamics to study the effects of dynamic interactions between dislocations and defects on the anticipated NLUS responses via β.

REFERENCES

[1] M. J. Whittle, Insight **51**(3), 140 (2009).

[2] K. H. Matlack, J.-Y. Kim, L. J. Jacobs, and J. Qu, J. Nondestruct. Eval. **34**(1), 273 (2014).

[3] R. B. Thompson and H. F. Tiersten, J. Acoust. Soc. Am. **62**(1), 33 (1977).

[4] K. H. Matlack, J. Y. Kim, J. J. Wall, J. Qu, L. J. Jacobs, and M. A. Sokolov, J. Nucl. Mater. **448**(1–3), 26 (2014).

[5] C. J. Lissenden, Y. Liu, G. W. Choi, and X. Yao, J. Nondestruct. Eval. **33**(2), 178 (2014).

[6] B. Wu, B. S. Yan, and C. F. He, Trans. Nonferr. Met. Soc. **21**(12), 2597 (2011).

[7] J. H. Cantrell, J. Appl. Phys. **105**(4), 043520 (2009).

[8] J. H. Cantrell, J. Appl. Phys. **106**(9), 093516 (2009).

[9] J. H. Cantrell, Philos. Mag. **86**(11), 1539 (2006).

[10] J. H. Cantrell, Proc. Roy. Soc. A Math. Phys. Eng. Sci. **460**(2043), 757 (2004).

[11] D. C. Price and D. A. Scott, AIP Conf. Proc. **657**, 1567 (2003).

[12] J. H. Cantrell and W. T. Yost, Appl. Phys. Lett. **77**(13), 1952 (2000).

[13] J. H. Cantrell and W. T. Yost, J. Appl. Phys. **81**(7), 2957 (1997).

[14] J. H. Cantrell and W. T. Yost, Philos. Mag. A **69**(2), 315 (1994).

[15] J. F. Zhang, S. Li, F. Z. Xuan, and F. Yang, Mater. Sci. Eng. A **622**, 146 (2015).

[16] Y. X. Xiang, M. X. Deng, and F. Z. Xuan, J. Nondestruct. Eval. **33**(2), 279 (2014).

[17] S. Punnose, A. Mukhopadhyay, R. Sarkar, and V. Kumar, Mater. Sci. Eng. A **607**, 476 (2014).

[18] J. F. Zhang, F. Z. Xuan, Y. X. Xiang, and F. Q. Yang, Mater. Sci. Technol. **29**(11), 1304 (2013).

[19] S. Y. Hu, Y. L. Li, J. McCloy, R. Montgomery, and C. H. Henager, Magn. Lett. IEEE **4**, 3500104 (2013).

[20] S. T. Abraham, S. K. Albert, C. R. Das, N. Parvathavarthini, B. Venkatraman, R. S. Mini, and K. Balasubramaniam, Acta Metall. Sin. **26**(5), 545 (2013).

[21] C. S. Kim, Mater. Trans. **53**(11), 2028 (2012).

[22] K. H. Matlack, J. J. Wall, J. Y. Kim, J. Qu, L. J. Jacobs, and H. W. Viehrig, J. Appl. Phys. **111**(5), 054911 (2012).

[23] C. Kim and I. Park, J. Nucl. Sci. Technol. **45**(10), 1036 (2008).

[24] A. Hikata, B. B. Chick, and C. Elbaum, J. Appl. Phys. **36**(1), 229 (1965).

[25] J. H. Cantrell and X. G. Zhang, J. Appl. Phys. **84**(10), 5469 (1998).

[26] Y. U. Wang, Y. M. Jin, A. M. Cuitino, and A. G. Khachaturyan, Philos. Mag. Lett. **81**(6), 385 (2001).

[27] C. Shen and Y. Wang, Acta Mater. **51**(9), 2595 (2003).

[28] S. Y. Hu, Y. L. Li, Y. X. Zheng, and L. Q. Chen, Int. J. Plast. **20**(3), 403 (2004).

[29] P. A. Geslin, B. Appolaire, and A. Finel, Appl. Phys. Lett. **104**(1), 011903 (2014).

[30] S. L. Zheng, D. C. Zheng, Y. Ni, and L. H. He, NPJ Comput. Mater. **4**(1), 20 (2018).

[31] L. Q. Chen, Annu. Rev. Mater. Res. **32**, 113 (2002).

[32] J. J. Rushchitsky, *Nonlinear Elastic Waves in Materials* (Springer International Publishing, 2014).

[33] B. F. Apostol, Phys. Lett. A **318**(6), 545 (2003).

[34] T. Mura, *Micromechanics of Defects in Solids* (Springer, 1987).

[35] P. J. Othen, M. L. Jenkins, and G. D. W. Smith, Philos. Mag. A **70**(1), 1 (1994).

[36] S. Y. Hu, C. H. Henager, Y. L. Li, F. Gao, X. Sun, and M. A. Khaleel, Model. Simul. Mater. Sci. Eng. **20**(1), 015011 (2012).

[37] Y. L. Li, S. Y. Hu, C. H. Henager, H. Q. Deng, F. Gao, X. Sun, and M. A. Khaleel, J. Nucl. Mater. **427**(1–3), 259 (2012).

[38] L. Q. Chen and J. Shen, Comput. Phys. Commun. **108**(2–3), 147 (1998).

[39] S. Y. Hu and L. Q. Chen, Acta Mater. **49**(11), 1879 (2001).

[40] C. Cattani, J. J. Rushchitsky, and S. V. Sinchilo, Int. Appl. Mech. **40**(2), 183 (2004).

[41] R. Monzen, M. L. Jenkins, and A. P. Sutton, Philos. Mag. A **80**(3), 711 (2000).

[42] S. Y. Hu, Y. L. Li, and K. Watanabe, Model. Simul. Mater. Sci. Eng. **7**(4), 641 (1999).

[43] Y. L. Li, S. Y. Hu, X. Sun, and M. Stan, NPJ Comput. Mater. **3**(1), 16 (2017).

[44] W. Setyawan, C. H. Henager, Jr., and S. Y. Hu, J. Appl. Phys. **124**(3), 035104 (2018).

[45] K. Scott, J. Y. Kim, J. J. Wall, D. G. Park, and L. J. Jacobs, NDT&E Int. **89**, 40 (2017).

[46] G. J. Ackland, D. J. Bacon, A. F. Calder, and T. Harry, Philos. Mag. A **75**(3), 713 (1997).

[47] C. Domain and C. S. Becquart, Phys. Rev. B **65**(2), 024103 (2002).

[48] W. Klement, Trans. Metall. Soc. AIME **233**(6), 1180 (1965); available at http://www.aimehq.org/doclibrary-assets/search/docs/Volume%20233/233-215.pdf.

[49] F. Maury, N. Lorenzelli, M. H. Mathon, C. H. Denovion, and P. Lagarde, J. Phys. Condens. Matter **6**(2), 569 (1994).